ADVANCED OPTICAL MATERIALS
www.advopticalmat.de

Breaking the Diffraction Limit with Radially Polarized Light Based on Dielectric Metalenses

Ruizhi Zuo, Wenwei Liu, Hua Cheng, Shuqi Chen,* and Jianguo Tian*

Dielectric metalenses with high efficiency and compact size have been widely investigated recently, but still suffer from Abbe diffraction limit. Herein, with linear polarization incidence, a dielectric metalens is demonstrated to efficiently generate and focus radially polarized light simultaneously. Two novel methods are proposed to achieve super-resolution. First, a circular high-pass aperture is utilized to enhance the longitudinal field component in the vicinity of focus with the focal spot size of $0.138\lambda^2$, much smaller than the theoretical limit of $0.212\lambda^2$. The key parameters that impact the focusing size are explored in detail, such as radius of the circular aperture and numerical aperture of the metalens. Second, an extra phase distribution is added on the metalens to filter the transversely polarized component, which leads to a focal spot size of $0.144\lambda^2$. The approach provides a wide platform for sub-resolution focusing and imaging, which offers the capability of subdiffraction techniques for microscopy systems and information processing with extensive channels.

All-dielectric metasurface, an artificial electromagnetic platform composed of transparent dielectric building blocks in which light does not couple to plasmons or optical phonons, has attracted significant interest due to its abundant electromagnetic reply and low dissipation loss.[1–6] Owing to the precise control of wave front, various kinds of dielectric metasurfaces have been proposed in the applications such as Fano resonances,[7] electromagnetically induced transparency[8] negative-index responses and zero-index responses,[9,10] beam shaping,[11–13] holograms,[14] and structural color.[15,16] Recently, metalens, as a kind of metasurface based on complete phase modulation, has attracted lots of attention and offers a promising route to applications in interdisciplinary areas including imaging, spectroscopy, and lithography.[17–19] High numerical aperture (NA) metalens with high efficiency have been demonstrated in near-infrared[20] and visible frequencies,[21,22] which suggested potential intriguing possibilities of metalenses in commercial imaging systems. Achromatic metalenses have also been reported with multiwavelengths[23,24] and continuous bandwidth.[25] A 3D Luneburg lens at optical frequencies was demonstrated with an ideal focusing ability.[26] Recently, a wide-angle metalens that can perform Fourier transform was realized, which proved the capabilities of mathematical operations with arrays of nanoparticles.[27] However, the resolution of such metalenses is still limited by theoretical Abbe limit since their design principles are based on scalar diffractive optics.

Light beam with spatially inhomogeneous distributed polarization states, also known as vector beam, plays a critical role in many optical systems. Radially polarized light (RPL) has been investigated for many years in both conventional optics[28,29] and metasurfaces[30,31] due to its great potential in optical trapping, data storage, quantum dots, and so on. Since the diffraction of vector beams includes different electric components related to the propagation direction, the focal points of vector beams are not limited to the scalar diffraction–based Abbe limit. Several methods have been proposed to break the diffraction limit based on vector beams especially RPL. For example, an annular aperture was utilized to get tight RPL focusing with long depth of focus (DOF).[32,33] A parabolic mirror with high NA has also been demonstrated, which can focus RPL to a diffraction-limited dot at the visible.[34,35] In addition, by using an additional phase modulation, such as two discrete phase 0 and π, the full-width at half maximum (FWHM) of focal point can be reduced according to theoretical calculation.[36] The abovementioned methods are based on traditional optical media, which suffers from bulky size, limited capability of phase and polarization modulation, and weak strength of light-matter interaction. In recent years, some metasurfaces have been designed to transform the linearly polarized light or circularly polarized light to RPL,[29,37,38] and vice versa. Although phase and polarization of light beams can both be modulated through metasurfaces,[12] super-resolution with RPL based on a single-layer metalens has not been realized due to the absence of studying simultaneous control of RPL generation and focusing.

In this study, we demonstrate a single-layer metalens to generate and focus RPL simultaneously based on elliptic silicon post arrays. We realize super-resolution with two different methods by applying a circular aperture (CA) and additional phase distribution to the metalens, respectively. The CA is

Dr. R. Zuo, Dr. W. Liu, Prof. H. Cheng, Prof. S. Chen, Prof. J. Tian
The Key Laboratory of Weak Light Nonlinear Photonics
Ministry of Education
School of Physics and TEDA Institute of Applied Physics
Nankai University
Tianjin 300071, China
E-mail: hcheng@nankai.edu.cn; schen@nankai.edu.cn
Prof. H. Cheng, Prof. S. Chen, Prof. J. Tian
The Collaborative Innovation Center of Extreme Optics
Shanxi University
Taiyuan, Shanxi 030006, China
The ORCID identification number(s) for the author(s) of this article can be found under https://doi.org/10.1002/adom.201800795.

DOI: 10.1002/adom.201800795

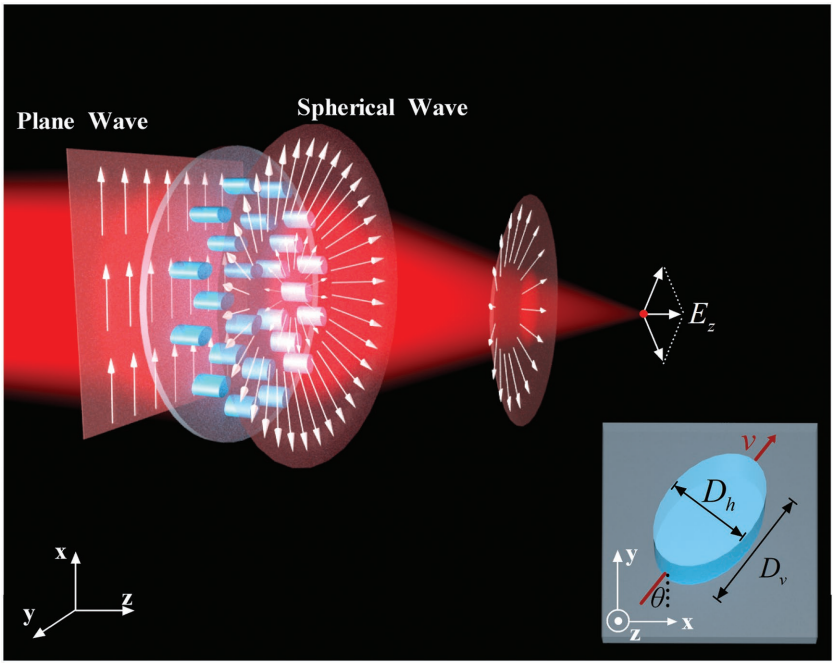

Figure 1. Schematic illustration of designed dielectric metalens illuminated with *x*-polarized light. Inset: Schematic view of unit cell: D_h and D_v are diameters of the elliptical cylinder, and rotation angle θ is the angle between *v*-axis and *y*-axis.

utilized to enhance the intensity of longitudinal electric component at the focus, and the additional phase distribution is to decrease the intensity of transversely polarized component in the vicinity of the focus resulting from electric destructive interference. The impacts of different NA on focal size and DOF are also discussed. The platform we proposed significantly decreases the focusing FWHM, and paves the way for super-resolution of imaging on a compact size.

A schematic illustration of the transmissive dielectric metalens that generates and focuses the RPL simultaneously at wavelength of 915 nm is shown in **Figure 1**. The building blocks of the metalens are amorphous silicon nanoposts with height of 715 nm and different orientation θ and diameters $\{D_h, D_v\}$. The refractive indices of amorphous silicon and silica substrate are 3.56 and 1.45 at 915 nm, respectively. It has been demonstrated that high-ratio silicon nanoposts in the near infrared can independently and arbitrarily control phase and polarization of light beams with high transmittance at the subwavelength scale.[12] We utilized similar silicon nanoposts to realize the required hyperbolic focusing phase distribution with $\varphi = \frac{2\pi}{\lambda}\left(\sqrt{r^2+f^2}-f\right)$, and radially polarization distribution with $\vec{p} = [\cos\alpha, \sin\alpha]^T$ simultaneously, where λ, f, r, α are the working wavelength in free space, designed focal length, central position of each unit cell, polarization angle ($\alpha = \arctan(y/x) + H(-x)\pi$, where $H(x)$ is the Heaviside step function), respectively. The electric transmission matrix of the subwavelength silicon unit cells can be expressed using a symmetric and unitary Jones matrix:

$$T = \begin{bmatrix} T_{xx} & T_{xy} \\ T_{yx} & T_{yy} \end{bmatrix} \quad (1)$$

and the transmitted electric field can be written as $E^{out} = TE^{in}$, where $E^{in} = [1, 0]^T$ and E^{out} are the incident and the transmissive electric field, respectively. For a given $E^{out} = e^{-i\varphi}[\cos\alpha, \sin\alpha]^T$, the phase φ and polarization angle α of each unit cell can be determined by the geometrical parameters $\{\theta, D_h, D_v\}$ of the silicon post. Specifically, the different combination of $\{D_h, D_v\}$ determines the phase shift φ of the transmitted light, with the phase difference of *v*-direction and *h*-direction fixed as π for convenience. On the other hand, for *x*-polarized incidence, the transmitted light can be expressed as

$$T'(\theta)|X\rangle = (\beta_0 + \beta_1\cos 2\theta)|X\rangle + \beta_1 \sin 2\theta |Y\rangle \quad (2)$$

where β_0 and β_1 are the amplitudes of the co- and cross-polarized waves, respectively. Since $|\varphi_v - \varphi_h| = \pi$ means that each unit cell serves as a half-wave plate, we have $\beta_0 = 0$ and $\beta_1 = 1$ in Equation (2). Thus, we obtain

$$\begin{aligned} T'(\theta)|X\rangle &= \cos 2\theta |X\rangle + \sin 2\theta |Y\rangle \\ &= [\cos 2\theta, \sin 2\theta]^T \end{aligned} \quad (3)$$

which means the transmitted wave is linearly polarized and the polarization angle $\alpha = 2\theta$.

According to the above method, we simulated and chose the shapes, orientation angles, and locations of every unit cell from a given E^{out}. Then, we utilized these silicon nanoposts to realize RPL generation and focusing simultaneously. The silicon nanoposts are designed as concentric rings on a silica substrate (Figure 1). The *n*th ring, with radius of $650 \times n$ nm, has $4 \times n$ unit cells, which are separated evenly along the ring. The metalens has 30-ring unit cells, in other words, the total amount of unit cells is 1860. The detailed design of silicon nanoposts will be discussed in the next part. Since the distance between adjacent silicon nanoposts is at the subwavelength scale, this arrangement of unit cells can avoid diffraction of light into nonzero diffraction orders and can facilely achieve the required phase and polarization distribution of the metalens with high NA.

To show the capability of the nanoposts for simultaneous modulating phase and polarization, we simulated magnetic and electric field intensity distributions of one of the silicon nanoposts with $D_h = 264$ nm and $D_v = 168$ nm based on Finite Element Modeling method in **Figure 2**a,b. The blue arrows represent the displacement current density, indicating the induced magnetic waveguide mode of high-ratio dielectric nanoposts.[22,39] The light is well confined in the nanoposts and the coupling between adjacent nanostructures is weak, which enables independent modulation of phase and polarization with a single unit cell. We also simulated the electric field component E_x distributions of the silicon post with different rotation angles, 0° and 90°, in Figure 2c. According to Equation (3), with a rotation angle $\theta = 90°$ of the nanopost, the polarization angle α is 180°, which equivalently indicates a π phase difference

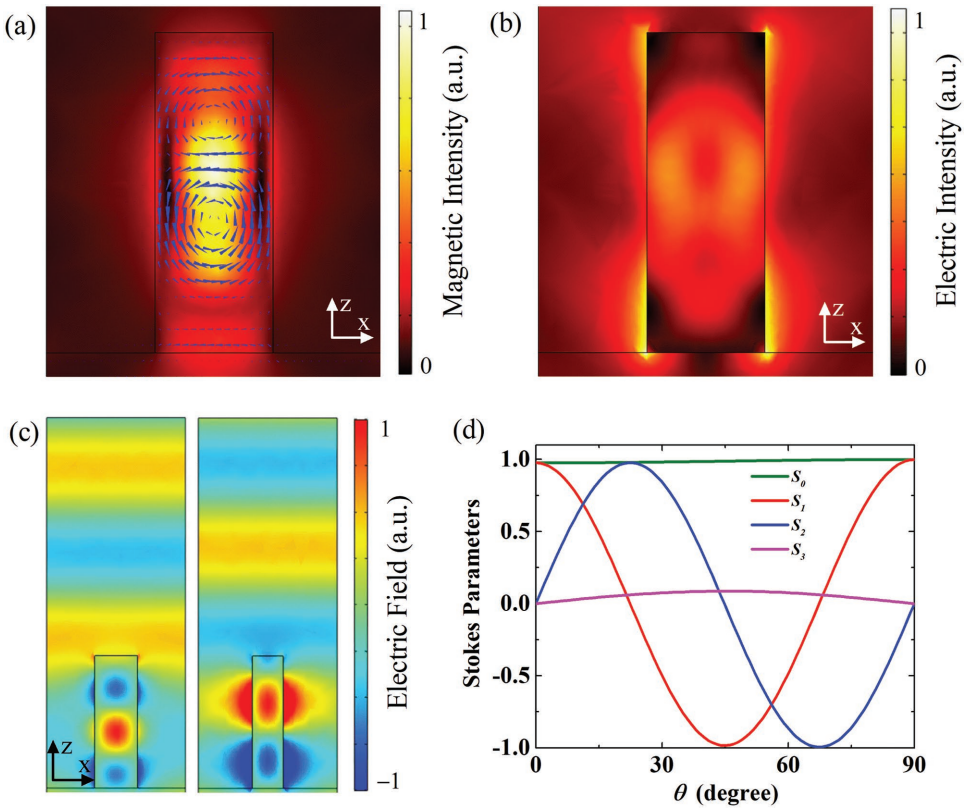

Figure 2. Simulated a) magnetic intensity and b) electric intensity of a nanopost with $D_h = 264$ nm and $D_v = 168$ nm under 915 nm incidence. The blue arrows indicate simulated snapshot of the displacement current densities. c) Simulated E_x distribution with $D_h = 264$ nm and $D_v = 168$ nm (left) and $D_h = 168$ nm and $D_v = 264$ nm (right) with $\theta = 0$. d) Stokes parameters of the transmitted field of nanopost with different rotation angle θ ranging from 0° to 90°.

of the electric field. The capability of polarization modulation of the nanoposts is described by the Stokes parameters in Figure 2d, where $S_0 = |E_x^2| + |E_y^2| \propto I$, $S_1 = |E_x^2| - |E_y^2|$, $S_2 = 2\mathrm{Re}(E_x E_y^*)$, and $S_3 = -2\mathrm{Im}(E_x E_y^*)$ (Re and Im represent the real and imaginary part of a complex number). With the rotation angle θ ranging from 0° to 90°, $S_3 \approx 0$ is maintained, which indicates that the transmitted light remains of linear polarization states and guarantees the RPL generation. The values of another two Stokes parameters S_1 and S_2 vary from −1 to 1, demonstrating the orientation angle of the linear polarization covers all the angles from 0° to 360°. This characteristic remains for all the selected half-wave-plate based nanoposts, the detailed $\{D_h, D_v\}$ of which are shown in **Table 1**.

Figure 3a,b shows the intensity and phase shift of transmitted light from 30 unit cells in different rings of the metalens with *x*-polarized and *y*-polarized incident light, respectively. A 3D finite-different time-domain method was utilized in our numerical simulation. The transmission is larger than 88% for both incident polarizations, which guarantees that the proposed platform maintains high transmission regardless of the rotation angle of the unit cells. Specifically, when illuminated with a normally *x*-polarized light, the metalens transforms the light

Table 1. Parameter setting and the corresponding phase for the selected nanoposts.

Post type	D_h [nm]	D_v [nm]	φ_h [π]	φ_v [π]	Post type	D_h [nm]	D_v [nm]	φ_h [π]	φ_v [π]
1	264	168	0.067	−0.905	16	168	256	−0.846	0.106
2	232	168	0.278	−0.674	17	224	168	0.396	−0.622
3	212	156	0.679	−0.362	18	152	216	−0.330	0.627
4	168	252	−0.816	0.128	19	308	76	0.905	−0.099
5	128	228	−0.197	0.791	20	252	168	0.128	−0.816
6	212	164	0.542	−0.472	21	164	224	−0.527	0.467
7	168	228	−0.648	0.327	22	168	308	0.792	−0.215
8	236	168	0.239	−0.701	23	264	168	0.067	−0.905
9	172	236	−0.845	0.216	24	168	224	−0.622	0.397
10	232	172	0.252	−0.810	25	220	140	0.747	−0.247
11	168	232	−0.674	0.278	26	264	168	0.067	−0.905
12	224	168	0.396	−0.622	27	168	212	−0.551	0.476
13	164	212	−0.472	0.542	28	168	308	0.792	−0.215
14	216	148	0.704	−0.296	29	260	168	0.086	−0.875
15	72	320	−0.095	0.919	30	164	224	−0.527	0.467

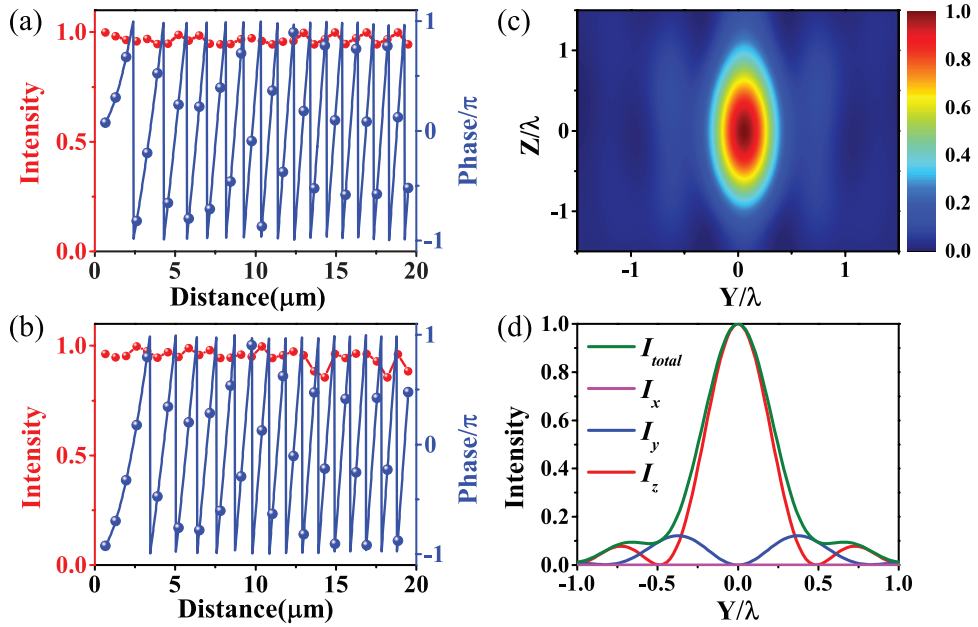

Figure 3. Designed metalens for transforming linearly polarized light to RPL and focusing it with focal length of 6 μm operating at wavelength of 915 nm and NA of 0.956. a,b) Simulated intensity (red dots) and phase (blue dots) and calculated phase (blue line) of transmission light from 30 unit cells at different locations illuminated with *x*-polarized light and *y*-polarized light, respectively. c) Simulated intensity distribution in the vicinity of focus in *y*–*z* plane. d) Line section ($z = 0$, $x = 0$) through the focal region showing the intensity profile of total field (FWHM = 484 nm) and each electric field component.

to RPL and focuses it to a spot whose FWHM is 484 nm (0.53λ) with focal length of 6 μm. The calculated NA of the metalens reaches 0.957, and the FWHM is close to the diffraction limit of 478 nm (0.52λ). The simulated focusing RPL are shown in Figure 3c,d. The longitudinal component (I_z) reveals a strong peak at the optical axis, whereas the transverse component (I_y) produces two weak peaks of intensity on each side of the axis. This phenomenon can be attributed to the diffraction between RPL rays propagating with opposite output angles, which possesses the same longitudinal components and the opposite transverse components, leading to a doughnut-shaped profile at the focal axis. The total intensity profile at the focus shows a single peak, which is wider than that of the longitudinal component. As a result, by reducing the two-peak-shaped transverse components, the total intensity profile approaches to the longitudinal component profile, and the FWHM of the focal point can be further decreased to realize a tight focusing that breaks the diffraction limit.

Since the RPL rays with smaller output angles possess larger transverse electric components, we optimized the metalens by employing a high-pass filtering CA at the center of the original metalens to suppress the transverse component near the focal point, as shown in **Figure 4**a. As a result, only waves propagating under large output angles to the optical axis contribute to the focal field. Therefore, the polarization essentially approaches to the optical axis, and size of the focus could be smaller than the Abbe limit due to the decrease of transverse components. For the convenience of the experimental realization, the CA can be realized just by a circular metal layer, such as a gold layer with thickness of about 100 nm. We define σ as ratio of the radii of the CA and the metalens to study the effects of CA on the FWHM of the focal point. As shown in Figure 4b,c, the simulated FWHM of the focus is reduced to 0.419λ (384 nm) with total spot size of 0.138λ^2, which is much smaller than that of the result without the CA in Figure 4d (FWHM = 0.53λ), and the beam area is reduced by 37%. The FWHM will decrease with the increasing of the σ. On the other hand, with the increasing of the σ, the DOF of the focus also increases. Interestingly, the DOF reaches 5.6λ when $\sigma = 0.67$, which is much longer than that of the result obtained by the original metalens without a CA (1.5λ). Since the polarization of the light on focus is mainly *z*-polarized, the long DOF focus is actually longitudinally polarized. Such an extension of optical field at the focal point is based on the inference between inner part and outer part rays in the region around the focal point. When the RPL generated from the metasurface with a small σ is focused, the incident angles of the two rays are significantly different. Therefore, constructive interference only appears at the focal plane because of the strong phase difference in other place. In contrast, when the metasurface has a large σ, the incident angles are almost the same and the phases of the rays match well. Thus, the input beam interferes constructively on the optical axis for a long distance along *z*-axis.

To show the impact of the NA on focusing, we simulated the metalenses with different radius but fixed $\sigma = 2/3$. As shown in **Figure 5**a, the CA can help the metalens to achieve super-resolution for different NA. The calculated FWHM of the metalens is about 85 nm smaller than the diffraction limit, and reaches 94 nm when NA = 0.957. We also calculated the energy ratio of the transverse component field to the total field around the focus for different NA. The results in Figure 5b show that the energy is more concentrated in the focus area when the NA

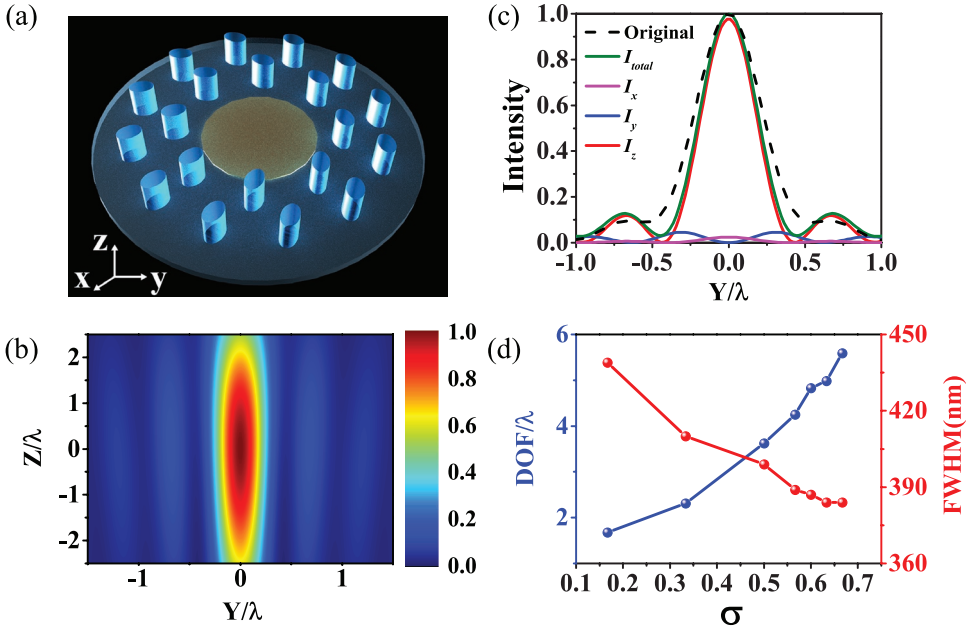

Figure 4. a) Schematic illustration of designed metalens for sub-resolution focusing with a CA in the center of the metalens. This illustration is only for general idea. In our setup, the metalens possesses 1020 unit cells. b) Simulated intensity distribution in the vicinity of focus in *y*–*z* plane. c) Line section ($z = 0$, $x = 0$) through the focal region showing the intensity profile of total field (FWHM = 384 nm) and each electric field component. d) Simulated DOF (blue-dot line) and FWHM (red-dot line) for different size of the CA, where σ is defined as the radio of the radii of the CA and the metalens.

increases, which demonstrates the principle proposed above, i.e., the outer part rays of focused RPL contributed more longitude component field than inner part rays.

Another efficient method to realize super-resolution is to add extra phase modulation on some unit cells instead of the transmission filter CA, as shown in **Figure 6**a. With delicate design of the extra phase distribution, the metalens works like a polarization filter to diffract the transverse components away from beam center more than the longitudinal field. The electric field components near the focus of RPL can be calculated according to the diffraction theory[28]:

$$E_z(r,z) = A\int_0^{\alpha} \cos^{1/2}\theta \sin(2\theta) l(\theta) J_1(kr\sin\theta) e^{ikz\cos\theta} d\theta \quad (4)$$

$$E_r(r,z) = 2iA\int_0^{\alpha} \cos^{1/2}\theta \sin^2(\theta) l(\theta) J_0(kr\sin\theta) e^{ikz\cos\theta} d\theta \quad (5)$$

where α = arcsin(NA). For plane wave incidence, we set $l(\theta) = e^{i\varphi(\theta)}$, where $\varphi(\theta)$ is the extra phase distribution as optimized in Figure 6b. When designing metalens with extra phase, we firstly calculated the intensity distribution around the focus to optimize the focusing result. We use the summing format of formulas (4) and (5) to obtain the optimized extra phase distribution since the nanoposts on the metalens are discrete. For all 30 concentric ring nanoposts, the nanoposts in the 4th–7th and 14th–17th rings are changed to those with extra phase of π but with the same polarization, as indicated by red and yellow marks in Figure 6a,b. Interestingly, we only need to rotate the silicon nanoposts by 90° to add extra π phase, which also means rotating the polarization by 180°. The simulated intensity distribution in the vicinity of the focus is shown in Figure 6c,d. The theoretical diffraction limit is 478 nm (0.52λ) and the calculated FWHM of the extra-phase metalens reaches 391.6 nm (0.428λ), which reduces the spot size by 32%. The sub-resolution focusing can be further improved by increasing the numbers of the unit cells and radius of the metalens. It should be mentioned that the realized sub-resolution is based on two extra phase 0 and π, which could also be improved by choosing other phase functions in the interval $-\pi$ to π. The two methods proposed in our study could be combined together if the nanoposts can simultaneously realize phase filter and intensity filter, which may realize the deep sub-resolution focusing. However, the corresponding optimization requires more computational cost, which is beyond the current scope of this study. To calculate the efficiency of the metalens, we set a

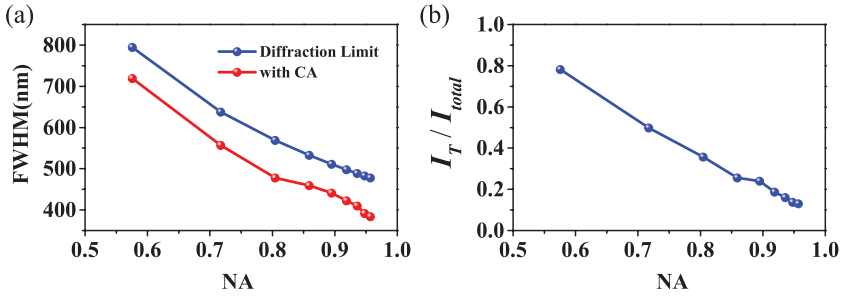

Figure 5. a) Comparison between diffraction limit (blue-dot line) and simulated FWHM (red-dot line) of the metalens with a CA for different NA. b) Intensity ratio between the transverse component and total field versus NA.

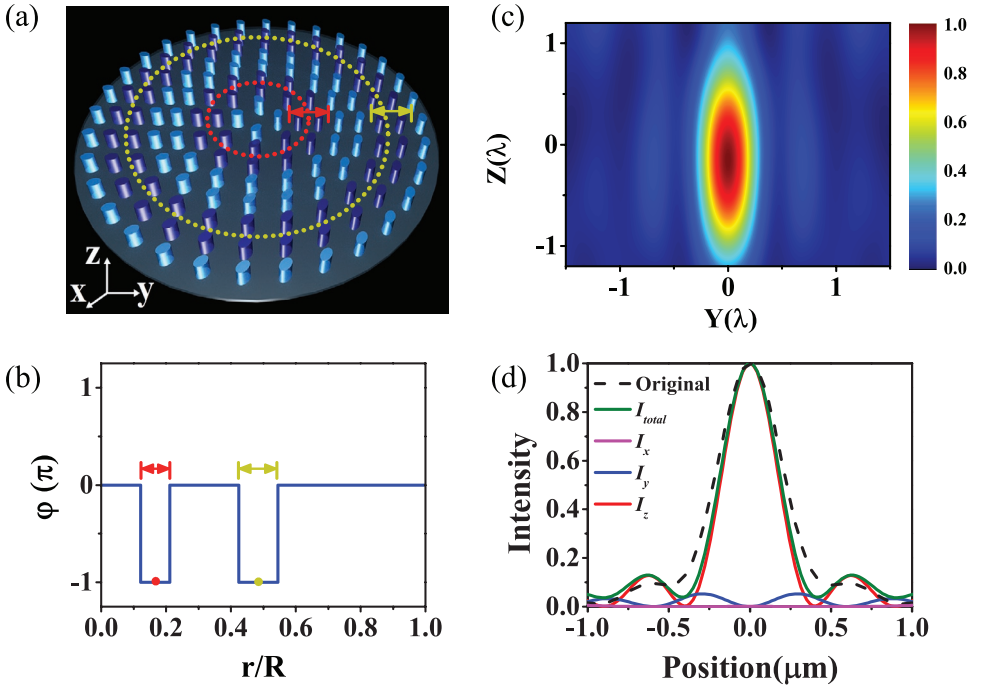

Figure 6. a) Schematic illustration of the designed metalens for sub-resolution with an extra phase distribution. The metalens consists of 1860 unit cells. The unit cells in the 4th–7th and 14th–17th rings have extra π phase shift compared with the origin phase design. b) Extra phase distribution for different position r of the metalens, which is normalized by the total radius R of the metalens. The red and yellow areas correspond to the nanopost groups indicated in (a). c) Simulated intensity distribution in the vicinity of focus in y–z plane. d) Line section ($z = 0$, $x = 0$) through the focal region showing the intensity profile of total field (FWHM = 391.6 nm) and each electric field component.

field monitor with size of 10 × 10 μm at the center of the focal plane, and normalized it with the total incident light. The calculated efficiency is 10.1% and 19.6% for the metalens with a CA and additional phase distribution, respectively. This could be attributed to two reasons. First, the size of the unit cells is not small enough, and the focusing profile can be further improved by using deep subwavelength nanostructures.[40] Second, the metalens with a high-pass filter or an additional phase distribution deviates from the ideal focusing lens, which is the price for the far-field sub-resolution focusing. If the image or the light source is bright enough, the limited efficiency of the metalens is tolerable in the practical applications.

We compared two sub-resolution designs for different incident wavelengths and incident angles. As shown in **Figure 7**a, for the metalens with a CA in the center, the FWHM of the focal point is smaller than the theoretical Abbe limit (0.52λ) in the waveband from 870 to 1130 nm. With the incident wavelength increasing, the FWHM decreases to 0.386λ under 1105 nm incidence. The intensity of the focal point reaches its maximum at around 961 nm, and the efficiency of the metalens decreases for other incident wavelength. This can be attributed to the destructive interference between different RPL at the focal spot for the incident wavelength departure from the designed one. For the metalens with an extra phase distribution, the sub-resolution behavior also reaches its optimization from 870 to 1130 nm. For incident wavelength larger than 1130 nm, the focal length is shorter than 3.9 μm leading to increasing near-field effects. We do not make further efforts to study such effects because we focus on far-field sub-resolution in this study, although near-field effects contain more evanescent components, which benefits the high resolution of the metalens.

We also simulated the intensity distribution for the two proposed methods with different incident angles. For the metalens with a CA in the center, the computed FWHM for 0°, 1°, 2°, 3°, 4°, 5° incidence is 0.42λ, 0.42λ, 0.43λ, 0.45λ, 0.49λ, 0.57λ, respectively. For the metalens with an extra phase distribution, the computed FWHM for 0°, 1°, 2°, 3°, 4°, 5°, 6° incidence is 0.43λ, 0.43λ, 0.44λ, 0.45λ, 0.46λ, 0.50λ, 0.57λ, respectively. According to the calculated results, the metalens with a CA in the center remains sub-resolution with an angle-of-view about 4.5° × 4.5°, while the metalens with an extra phase distribution possesses an angle-of-view about 5.5° × 5.5°. The intensity of the focal point will decrease with increasing the incident angles, which can be attributed to the diffraction phase mismatching for oblique incidence. This phase mismatching makes a curved focal plane, leading to the decreasing of the intensity in a flat cut-plane. This monochromatic aberration can be corrected by doublet metalens.[41]

In order to estimate the tolerance of the proposed design, we calculated the variation of the electric field $E_z = \int_0^\alpha d\theta p(\theta,r,z)e^{i\varphi_\theta}$ given in formula (4), where $p(\theta, r, z) = A\cos^{1/2}\theta\sin(2\theta)J_1(kr\sin\theta)e^{ikz\cos\theta}$. It should be noted that the fabricating error mainly lies in the phase factor $e^{i\varphi_\theta}$, because θ is insensitive to the fabrication error due to long focal length of the metalens, and $\{r, z\}$ are only coordinates in real space, which are irrelative to the fabrication. The variation of the phase factor $e^{i\varphi_\theta}$ is $\Delta e^{i\varphi_\theta} = ie^{i\varphi_\theta}\Delta_\theta$, where Δ_θ is the phase uncertainty due to fabrication deviation. Thus, we obtain

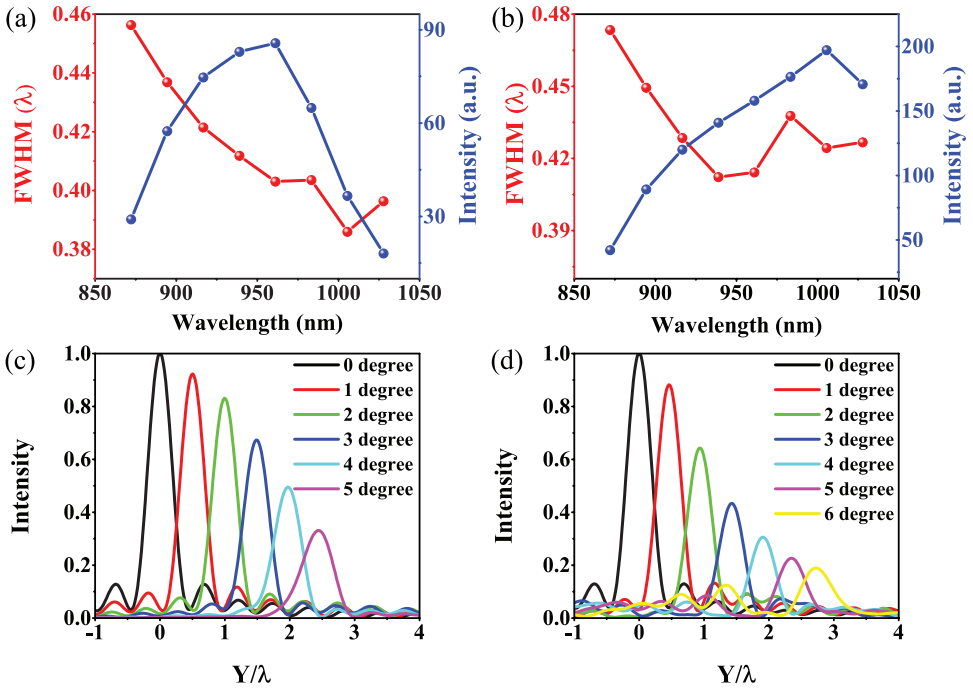

Figure 7. Calculated FWHM (red-dot line) and intensity (blue-dot line) of the focal point for different incident wavelengths for a) the metalens with a CA and b) the metalens with an extra phase distribution. Line section ($z = 0$, $x = 0$) in the focal plane showing the intensity profile of the total field for different incident angles for c) the metalens with a CA and d) the metalens with an extra phase distribution.

$$\frac{\Delta E_z}{E_z} = \frac{\int_0^\alpha d\theta p(\theta,r,z)e^{i\varphi_\theta} i\Delta_\theta}{\int_0^\alpha d\theta p(\theta,r,z)e^{i\varphi_\theta}} \tag{6}$$

Similarly, according to formula (5), we obtain

$$\frac{\Delta E_r}{E_r} = \frac{\int_0^\alpha d\theta q(\theta,r,z)e^{i\varphi_\theta} i\Delta_\theta}{\int_0^\alpha d\theta q(\theta,r,z)e^{i\varphi_\theta}} \tag{7}$$

where $q(\theta, r, z) = 2iA\cos^{1/2}\theta\sin^2\theta J_0(kr\sin\theta)e^{ikz\cos\theta}$. Interestingly, the integrating factor of numerator in Equations (6) and (7) can be divided into two parts. The first part is the integrating factor of E_z and E_r, and the other part is $i\Delta_\theta$. On the one hand, Δ_θ is randomly distributed, leading to destructive interference between each integrating factor of $p(\theta,r,z)e^{i\varphi_\theta}i\Delta_\theta$ or $q(\theta,r,z)e^{i\varphi_\theta}i\Delta_\theta$. Thus, $\Delta E_z/E_z$ ($\Delta E_r/E_r$) is limited. On the other hand, $|\Delta_\theta|$ can be reduced by improving the fabrication accuracy or by fabricating several samples and choosing the best one. The tolerance of the first kind of design (with a CA in the center of the metalens) can also be calculated according to the abovementioned analysis method, only with the integrating range replaced by $[\alpha_0, \alpha]$, where $\theta \in [0, \alpha_0)$ indicates the CA area.

In conclusion, we have proposed a dielectric metalens that can generate RPL and focus it to a subdiffraction focal spot simultaneously based on complete control of phase and polarization of light. Two methods are adopted to realize subresolution. On the one hand, with a CA placed in the center of the metalens to filter the lower spatial frequency of the optical field, the FWHM of focal spot can be reduced to 0.419λ which is smaller than the theoretical Abbe limit (0.52λ). As the FWHM of the focal spot is reduced, the DOF becomes longer than 5λ with a longitudinal polarized field distribution in the focal spot. The FWHM of the focal spot and DOF will respectively decrease and increase as the NA of the metalens increases. On the other hand, a focal spot size of 0.428λ can be achieved through a metalens with an optimized extra phase distribution added to the original phase design. Based on the principle proposed in this study, we can also efficiently generate and focus other vectorial fields simultaneously with a linearly polarized incident wave. The design principle proposed in this study is not only limited under the wavelength of 915 nm. Taking advantage of high-index and low-loss dielectric materials, which can independently and locally control phase and polarization of light, the sub-resolution design is also attainable with amorphous silicon in the other near infrared waveband, and with titanium dioxide or gallium nitride in the visible.[42] This novel and flexible method to achieve sub-resolution could widely benefit nanophotonic applications in optical manipulation, imaging, and microscopy. Further improvements are expected by using materials with optical nonlinearities, which might extend the resolution and provide tunability of the sub-resolution metalens design.

Acknowledgements

R.Z. and W.L. contributed equally to this work. This work was supported by the National Key Research and Development Program of China (Grant Nos. 2017YFA0303800 and 2016YFA0301102), the Natural Science Foundation of China (Grant Nos. 11774186, and 11574163), the Natural Science Foundation of Tianjin (16JCQNJC01700), and 111 Project (B07013).

Conflict of Interest

The authors declare no conflict of interest.

Keywords

diffraction limit, metalenses, metasurfaces, polarization, super-resolution

Received: June 19, 2018
Revised: July 24, 2018
Published online:

[1] S. Jahani, Z. Jacob, *Nat. Nanotechnol.* **2016**, *11*, 23.
[2] S. Chen, Z. Li, Y. Zhang, H. Cheng, J. Tian, *Adv. Opt. Mater.* **2018**, *6*, 1800104.
[3] L. Zhang, S. Mei, K. Huang, C.-W. Qiu, *Adv. Opt. Mater.* **2016**, *4*, 818.
[4] P. Genevet, F. Capasso, F. Aieta, M. Khorasaninejad, R. Devlin, *Optica* **2017**, *4*, 139.
[5] H.-T. Chen, A. J. Taylor, N. Yu, *Rep. Prog. Phys.* **2016**, *79*, 076401.
[6] A. I. Kuznetsov, A. E. Miroshnichenko, M. L. Brongersma, Y. S. Kivshar, B. Luk'yanchuk, *Science* **2016**, *354*, aag2472.
[7] Y. Zhang, W. Liu, Z. Li, Z. Li, H. Cheng, S. Chen, J. Tian, *Opt. Lett.* **2018**, *43*, 1842.
[8] Y. Yang, I. I. Kravchenko, D. P. Briggs, J. Valentine, *Nat. Commun.* **2014**, *5*, 5753.
[9] X. Huang, Y. Lai, Z. H. Hang, H. Zheng, C. T. Chan, *Nat. Mater.* **2011**, *10*, 582.
[10] P. Moitra, Y. Yang, Z. Anderson, I. I. Kravchenko, D. P. Briggs, J. Valentine, *Nat. Photonics* **2013**, *7*, 791.
[11] F. Aieta, P. Genevet, M. A. Kats, N. Yu, R. Blanchard, Z. Gaburro, F. Capasso, *Nano Lett.* **2012**, *12*, 4932.
[12] A. Arbabi, Y. Horie, M. Bagheri, A. Faraon, *Nat. Nanotechnol.* **2015**, *10*, 937.
[13] M. I. Shalaev, J. Sun, A. Tsukernik, A. Pandey, K. Nikolskiy, N. M. Litchinitser, *Nano Lett.* **2015**, *15*, 6261.
[14] X. Ni, A. V. Kildishev, V. M. Shalaev, *Nat. Commun.* **2013**, *4*, 2807.
[15] Z. -Z. Gu, H. Uetsuka, K. Takahashi, R. Nakajima, H. Onishi, A. Fujishima, O. Sato, *Angew. Chem., Int. Ed.* **2003**, *42*, 894.
[16] B. Yang, W. Liu, Z. Li, H. Cheng, S. Chen, J. Tian, *Adv. Opt. Mater.* **2018**, *6*, 1701009.
[17] A. Pros, M. G. Nielsen, R. L. Eriksen, S. I. Bozhevolnyi, *Nano Lett.* **2013**, *13*, 829.
[18] D. Fattal, J. Li, Z. Peng, M. Fiorentino, R. G. Beausoleil, *Nat. Photonics* **2010**, *4*, 466.
[19] M. Khorasaninejad, F. Aieta, P. Kanhaiya, M. A. Kats, P. Genevet, D. Rousso, F. Capasso, *Nano Lett.* **2015**, *15*, 5358.
[20] A. Arbabi, Y. Horie, A. J. Ball, M. Bagheri, A. Faraon, *Nat. Commun.* **2015**, *6*, 7069.
[21] M. Khorasaninejad, W. T. Chen, R. C. Devlin, J. Oh, A. Y. Zhu, F. Capasso, *Science* **2016**, *352*, 1190.
[22] M. Khorasaninejad, A. Y. Zhu, C. Roques-Carmes, W. T. Chen, J. Oh, I. Mishra, R. C. Devlin, F. Capasso, *Nano Lett.* **2016**, *16*, 7229.
[23] F. Aieta, M. A. Kats, P. Genevet, F. Capasso, *Science* **2015**, *347*, 1342.
[24] J. Hu, C. -H. Liu, X. Ren, L. J. Lauhon, T. W. Odom, *ACS Nano* **2016**, *10*, 10275.
[25] M. Khorasaninejad, Z. Shi, A. Y. Zhu, W. T. Chen, V. Sanjeev, F. Capasso, *Nano Lett.* **2017**, *17*, 1819.
[26] Y.-Y. Zhao, Y.-L. Zhang, M.-L. Zheng, X.-Z. Dong, X.-M. Duan, Z.-S. Zhao, *Laser Photonics Rev.* **2016**, *10*, 665.
[27] W. Liu, Z. Li, H. Cheng, C. Tang, J. Li, S. Zhang, S. Chen, J. Tian, *Adv. Mater.* **2018**, *30*, 1706368.
[28] K. S. Youngworth, T. G. Brown, *Opt. Express* **2000**, *7*, 77.
[29] L. Du, Z. Man, Y. Zhang, C. Min, S. Zhu, X. Yuan, *Sci. Rep.* **2017**, *7*, 41001.
[30] S. Chen, X. Zhou, Y. Liu, X. Ling, H. Luo, S. Wen, *Opt. Lett.* **2014**, *39*, 5274.
[31] J. Li, S. Chen, H. Yang, J. Li, P. Yu, H. Cheng, C. Gu, H.-T. Chen, J. Tian, *Adv. Funct. Mater.* **2015**, *25*, 704.
[32] R. Dorn, S. Quabis, G. Leuchs, *Phys. Rev. Lett.* **2003**, *91*, 233901.
[33] K. Kitamura, K. Sakai, S. Noda, *Opt. Express* **2010**, *18*, 4518.
[34] N. Davidson, N. Bokor, *Opt. Lett.* **2004**, *29*, 1318.
[35] J. Stadler, C. Stanciu, C. Stupperich, A. J. Meixner, *Opt. Lett.* **2008**, *33*, 681.
[36] H. Wang, L. Shi, B. Lukyanchuk, C. Sheppard, C. T. Chong, *Nat. Photonics* **2008**, *2*, 501.
[37] C. Pfeiffer, A. Grbic, *Phys. Rev. Appl.* **2014**, *2*, 044012.
[38] P. Yu, S. Chen, J. Li, H. Cheng, Z. Li, W. Liu, B. Xie, Z. Liu, J. Tian, *Opt. Lett.* **2015**, *40*, 3229.
[39] B. H. Chen, P. C. Wu, V. C. Su, Y. C. Lai, C. H. Chu, I. C. Lee, J. W. Chen, Y. H. Chen, Y. C. Lan, C. H. Kuan, D. P. Tsai, *Nano Lett.* **2017**, *17*, 6345.
[40] C. Wang, W. Liu, Z. Li, H Cheng, Z. Li, S. Chen, J. Tian, *Adv. Opt. Mater.* **2018**, *6*, 1701047.
[41] A. Arbabi, E. Arbabi, S. M. Kamali, Y. Horie, S. Han, A. Faraon, *Nat. Commun.* **2016**, *7*, 13682.
[42] W. T. Chen, A. Y. Zhu, V. Sanjeev, M. Khorasaninejad, Z. Shi, E. Lee, F. Capasso, *Nat. Nanotechnol.* **2018**, *13*, 220.